An Examination of the Wrangel Island Sea Ice Thickness Dipole

S. Ross[1,2], **G. W. K. Moore**[1,2]

[1]Department of Physics, University of Toronto, Toronto, Ontario, Canada

[2]Department of Chemical and Physical Sciences, University of Toronto - Mississauga, Mississauga, Ontario, Canada

Key Points:

- A reversal in ice motion in the Beaufort and Chukchi Seas can result in a sea ice thickness dipole in the vicinity of Wrangel Island
- The dipole is associated with a reversal in ice motion, wind direction and sea-level pressure anomalies across the western Arctic Ocean
- The dipole is the result of ice motion divergence and convergence across the region and may impact ocean circulation and ecosystems

Corresponding author: S. Ross, spenser.ross@utoronto.ca

Abstract

The Beaufort Sea High is a high-pressure system located in the Beaufort Sea and influences ocean circulation in the western Arctic known as the Beaufort Gyre. Wrangel Island, located in the western Chukchi Sea, typically experiences easterly sea ice motion due to the Beaufort Gyre. We find that under these climatological conditions, moving ice is blocked by the island and piles up on its eastern side, while ice on its western side continues to drift. This results in an ice thickness dipole across the island. A reversal in the sense of the oceanic and atmospheric circulation across the western Arctic results in a dipole with the opposing sign. We find the dipole is present throughout the year and is strongest in January when the ice thickness difference is approximately 1m. During the spring, it is associated with the transient opening of a polynya to the west of the island. The dipole is the result of opposing ice divergence and convergence across the western Arctic and may impact ocean circulation and ecosystems within the Chukchi Sea.

Plain Language Summary

The Arctic climate is rapidly changing with many important environmental consequences prompting increased scientific study. In this paper, we examine the interaction of drifting sea ice and Wrangel Island, which is located in the western Arctic Ocean's Chukchi Sea. We find that ice typically drifts from the east and is blocked by the island causing the ice to pile up on its eastern side. Ice continues to drift away from the western side of the island, thus a dipole in ice thickness is created. This dipole is present throughout the year and is strongest in January when the ice thickness difference is around 1m. We find that the formation of the dipole is associated with strong westward winds at the island. These winds are associated with a strong high-pressure system called the Beaufort Sea High that results in anti-cyclonic winds, ice motion and surface currents throughout the region. A reversal in the sense of the atmospheric circulations results in a dipole of opposing sign. The dipole is associated with ice thickness anomalies across the western Arctic and may impact ocean circulation and ecosystems across the region.

1 Introduction

The Arctic has seen significant changes in sea ice extent, thickness, and circulation over recent decades due to its changing climate. The Chukchi and Beaufort Seas are amongst the affected regions of the Arctic as a result of the rapid retreat of summer sea ice with important environmental and dynamical impacts (Frey et al., 2015; Timmermans & Pickart, 2023). As shown in Figure 1, the Beaufort Sea is located in the Western Arctic, north of Canada and Alaska. The Chukchi Sea is situated to the east of the Beaufort Sea, to the north of Siberia. These seas have seen intensifying ice cover decline since 2000, with surface winds driving a significant portion of this change (Frey et al., 2015). In addition to the overall ice cover decline, the Beaufort Sea has been transitioning from thicker multi-year ice to thinner first-year ice over the past decade (Moore et al., 2022). There is, however, inter-annual variability in the decline of ice cover and thickness, for example, Moore et al. (2022) found that in the summers of 2020 and 2021, the Beaufort Sea had anomalous amounts of thick, old ice. Sea ice advection contributed to this anomaly, including ice transport from the Chukchi Sea.

High sea-level pressure in the Beaufort Sea region, known as the Beaufort Sea High (BSH), strongly influences regional surface winds, ice motion and oceanic circulation in the western Arctic Ocean (Serreze & Barrett, 2011). The BSH is a closed anticyclone in the long-term annual mean as well as during the spring; while in other months it is characterized by a ridge extending over the Arctic Ocean from the Siberian High (Serreze & Barrett, 2011). The BSH is a crucial factor for major teleconnections including the Pacific-North American pattern, the Arctic dipole anomaly, and the Pacific decadal oscillation (Serreze & Barrett, 2011; Serreze & Barry, 2014).

Ocean and sea ice circulation in the region are driven by surface winds linked to prevailing high and low sea-level pressure centers (Timmermans & Toole, 2023). The Western Arctic oceanic circulation system is called the Beaufort Gyre and is driven by the anti-cyclonic circulation due to BSH-induced surface winds (Timmermans & Toole, 2023).

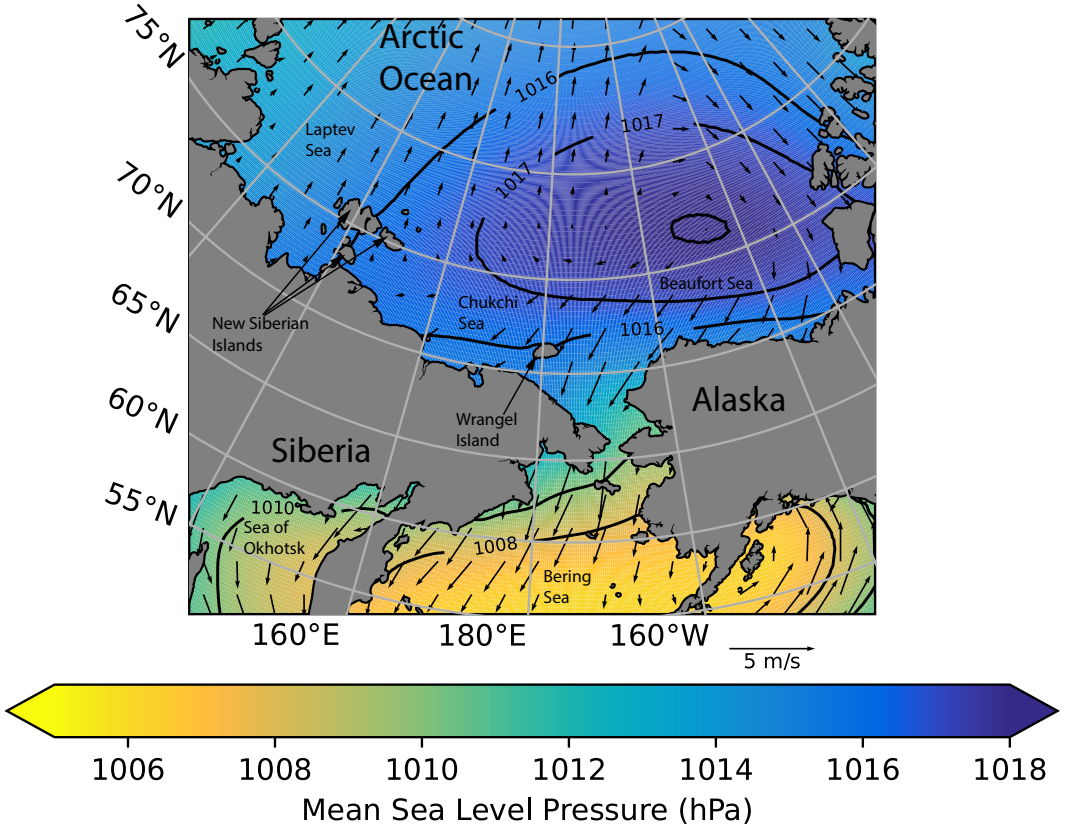

Figure 1. Annual mean sea-level pressure field from the ERA5 reanalysis 1979-2022. Vectors show annual mean ERA5 reanalysis 10m wind over the same period. Geographic locations mentioned in the paper are also indicated.

The BSH is thus critical to the movement of sea ice and surface currents throughout the western Arctic. As the climate changes, there have been multiple instances of BSH collapse causing a reversal in the Beaufort Gyre circulation. A warm autumn of 2016 led to thin sea ice and an anomalous thermal low in the Barents Sea allowing the intrusion of low-pressure systems from the North Atlantic into the western Arctic during the following winter(Moore et al., 2018; Babb et al., 2020). This caused a reversal in surface winds and sea ice motion across the western Arctic during the winter of 2017. Anomalously low sea-level pressure in the Beaufort Sea region has recurred in the recent decade, including another collapse in 2020 (Ballinger et al., 2021). Here, the collapse of the BSH and enhanced storminess in the winter of 2020 contributed to the reversal of the Beaufort Gyre. These reversals can have many consequences in ocean and ice motion, ice melt, weather, and other biological impacts (Ballinger et al., 2021; Babb et al., 2020; Moore et al., 2018).

Many regions of the western Arctic are impacted by variability in the Beaufort Gyre. As shown in Figure 1, the New Siberian Islands are located north of Siberia and between the Laptev and East Siberian Seas. The Laptev Sea hosts several polynyas including the Great Siberian Polynya which forms to the south-east of the Laptev Sea near the New Siberian Islands (UN Environment, 2015). These polynyas have great biological and ecological significance, thus changing sea ice circulation and concentration could have strong impacts on marine life in the region. The East Siberian Sea is an important region for sea ice circulation as ice originating here is advected into the Transpolar Drift Stream or the Beaufort Gyre (Pfirman, 2004).

Wrangel Island is located in the western Chukchi Sea to the north of the Bering Strait between Siberia and Alaska (shown in Figure 1). Wrangel Island has many important characteristics, including that it is a critical denning location for the Chukchi Sea subpopulation of polar bears. (LaRue & Stapleton, 2018). It is also home to a large population of Pacific walrus and other pinnipeds and marine mammals (Claudino-Sales,

2019; Hamilton et al., 2022). All of these populations and the complex food webs that support them are impacted by variability and trends in sea ice cover (Chinn et al., 2023; Jay et al., 2012).

As the island is situated just off the southwestern boundary of the Beaufort Gyre (Timmermans & Toole, 2023), its connection with ocean and ice circulation reveals notable phenomena. The typical anti-cyclonic circulation induces easterly winds from the Beaufort Sea towards the Chukchi Sea which contribute to westward transport of sea ice toward Wrangel Island. Much of the ice is blocked by the island which contributes to the opening of a seasonal polynya to its north-west (Sverdrup, 1929; Cavalieri & Martin, 1994; Moore & Pickart, 2012).

On the eastern side of Wrangel Island, blocked westward-flowing sea ice accumulates, which increases sea ice thickness and creates pressure ridges. Indeed, Wrangel Island, along with the New Siberian Islands, has the Arctic Ocean's highest frequency of leads and pressure ridges (Hutter et al., 2019; Willmes & Heinemann, 2015). Fascinatingly, these pressure ridges near Wrangel Island were documented over 100 years ago during the voyage of the "Karluk" (Chafe, 1918). During the Canadian Arctic Expedition to the western Arctic, in the fall of 1913, the Karluk became trapped in sea ice off of Alaska, it drifted westwards and eventually sank close to Wrangel Island in January 1914. The crew set up an ice camp and eventually sought refuge on Wrangel Island. They describe running into a series of pressure ridges and spent nearly a week cutting through them to reach the island (Chafe, 1918). While their exact measurement of these ridges is likely not exact, the early documentation of this ice accumulation at Wrangel Island is quite intriguing.

As we will show, this interaction of flowing ice and the island creates a dipole effect in ice thickness. That is anomalies in ice thickness of opposing signs and approximately the same magnitude. Under usual conditions, the anti-cyclonic Beaufort Gyre sends westward-flowing ice towards Wrangel Island, where it accumulates on its eastern

side. This creates a region of increased ice thickness on the island's east side and a region of decreased ice thickness to its west. During BSH collapses, this dipole can reverse as westerly winds drive eastward-flowing ice, which accumulates on the western side of the island (Moore et al., 2022).

In this paper, we analyze the Wrangel Island sea ice thickness dipole. We seek to quantify its seasonal strength, examine its various causes, and investigate its relationship with the BSH. For this analysis, we use in-situ surface data, reanalyses, and a coupled ice-ocean model.

2 Data and Methods

To analyze surface wind fields, we use ERA5 10m monthly averaged wind data. This monthly averaged data is available at ∼30 km resolution (Copernicus Climate Change Service, 2019). The ERA5 model is the fifth generation reanalysis based on the ECMWF's Integrated Forecast System (IFS) (Hersbach et al., 2020). The dataset is based on Cycle 41r2 of the IFS and uses a 4Dvar data assimilation system (Hersbach et al., 2020; Bonavita et al., 2016). For this investigation, we use ERA5 reanalysis monthly mean sea-level pressure and 10m wind data from 1979-2022 for the months of January, March, April, June, September, and November to capture seasonal variability throughout the year.

We validate the use of the ERA5 wind data by comparing the monthly averaged 10m zonal component of the wind to station observations at Wrangel Island. The station at Wrangel Island is called Ostrov Vrangelya and is located at 70.98°N, 178.65 °W at an elevation of 4m. Sea-level pressure, temperature, and wind data are available starting in November 1934 at a 6-hour interval from NOAA's International Summary of the Day (Smith et al., 2011; NOAA National Centers for Environmental Information, 2001). The results of the comparison are shown in Figure 2. There is general agreement between the monthly mean ERA5 zonal wind data and the observations at Wrangel Island from 1979-2022 throughout the year. There is, however, an underestimation of high-speed winds

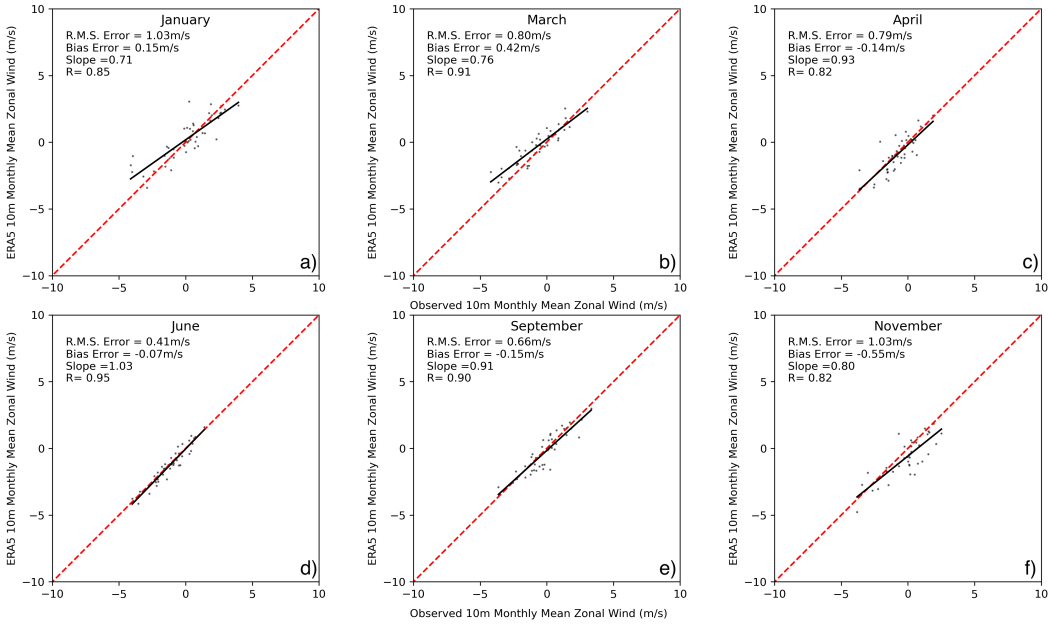

Figure 2. Scatter-plots of monthly mean zonal winds from the ERA5 reanalysis vs. observations at Wrangel Island. Data from 1979-2022 was used. Each figure has fit statistics including R.M.S error, bias error, slope, and the correlation "R" value.

(in either direction) in the fall and winter denoted by a decreased slope and an increased R.M.S Error (Figure 2 a, b, e).

The analysis of sea ice concentration, thickness, motion, advection, and production is based on the Pan-Arctic Ice Ocean Modeling and Assimilation System (PIOMAS) (Zhang & Rothrock, 2003). PIOMAS is calibrated with sea ice thickness observations and assimilates satellite sea ice concentration and sea surface temperature data (Schweiger et al., 2011; Zhang & Rothrock, 2003). Sea ice motion from PIOMAS is calibrated and validated through sea ice drift data (Schweiger & Zhang, 2015; Zhang et al., 2012) and the International Arctic Buoy Program (IABP) (Rigor et al., 2002). PIOMAS is forced by NCEP–NCAR reanalysis surface forcing atmospheric data (Zhang & Rothrock, 2003; Kalnay et al., 1996). Data from the National Snow and Ice Data Center (NSIDC) is also used to examine sea ice motion (Tschudi & Univ Of CO, 2019). To produce the ice mo-

tion data, gridded satellite imagery from several sources, winds from reanalyses, and buoy position data are combined through an optimal interpolation scheme (Tschudi et al., 2020). The satellite sources include the SMMR, SSM/I, and SSMIS instruments using both 37GHz and 85–91GHz channels. The spatial resolution of these sources is 25km resolution for the 37GHz fields and a 12.5km resolution for the 85–91GHz fields (Tschudi et al., 2020). The reanalysis wind forcing is derived from the NCEP-NCAR reanalysis dataset (Tschudi et al., 2020). The buoy position data is from the IABP (Rigor et al., 2002). For this analysis, we use monthly mean PIOMAS and NSIDC sea ice motion data, as well as PIOMAS sea ice thickness, advection, and production data from 1979-2022.

3 Results

Figure 3 shows monthly mean ERA5 zonal wind data at Wrangel Island from 1979-2022 for six months throughout the year. The least squares fit line demonstrates the trend in the U-component of the wind at Wrangel Island over time. The trend is increasing for January, March, April, and November (Figure 3 a, b, c, f). The trend is decreasing in June and September (Figure 3 d, e). However, no trend has statistical significance through a Student's T-test or a Mann-Kendall test at a 95% confidence level (Student, 1908; Mann, 1945; Kendall, 1948). In this figure, positive (negative) zonal wind values represent westerly (easterly) winds. Each month in Figure 3 indicates that there are, on the monthly mean timescale, reversals in the direction of the zonal wind. We expect easterly winds during the spring and over the long-term average from Wrangel Island as it lies near the southwest boundary of the Beaufort Gyre (Serreze & Barrett, 2011; Timmermans & Toole, 2023). These reversals in zonal wind direction may have connections to low BSH events and reversals of the Beaufort Gyre as has been documented to occur in 2017 and 2020 (Ballinger et al., 2021; Babb et al., 2020; Moore et al., 2018).

The wind data in Figure 3 were detrended by subtracting the trendline. The detrended data is shown in Figure 4. From the detrended data for each month, we deter-

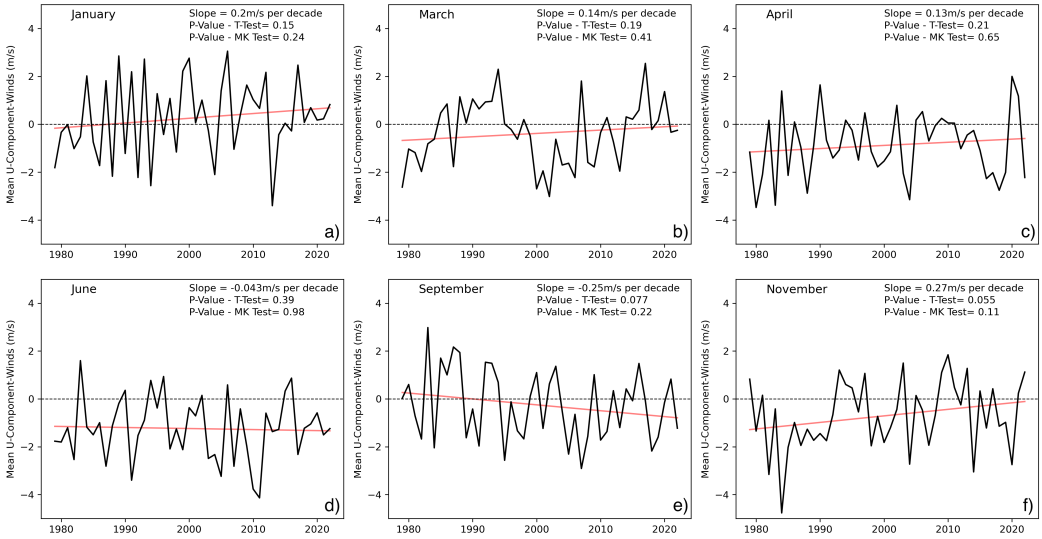

Figure 3. ERA5 monthly averaged zonal 10m winds (m/s) at Wrangel Island from 1979-2022 for various months. The red line indicates the least-squares best fit. The fit slope and significance testing p-values are included as well.

mined the top 25% of the years of strongest easterly and westerly monthly mean winds. These years are denoted in Figure 4 by black circle markers. With these dates, we used monthly averaged ice thickness data to identify composite ice characteristics associated with easterly and westerly winds throughout the year. The difference between the composites for the strongest easterly and westerly winds was then used to identify the Wrangel Island sea ice dipole. As calculated, the sign of the anomaly in any geophysical field corresponds to conditions during climatological easterly flow. A reversal in the circulation would result in a flipping of the sign of any anomaly. The results were insensitive to the thresholds used to identify extreme events.

Figure 5 shows the difference in monthly mean ice concentration across the Western Arctic between the months of strong easterly and westerly winds at Wrangel Island. In the winter there is no signal in the ice concentration at the island (Figure 5 a, b, c). There are ice concentration signals in the Bering Sea and the Sea of Okhotsk in those

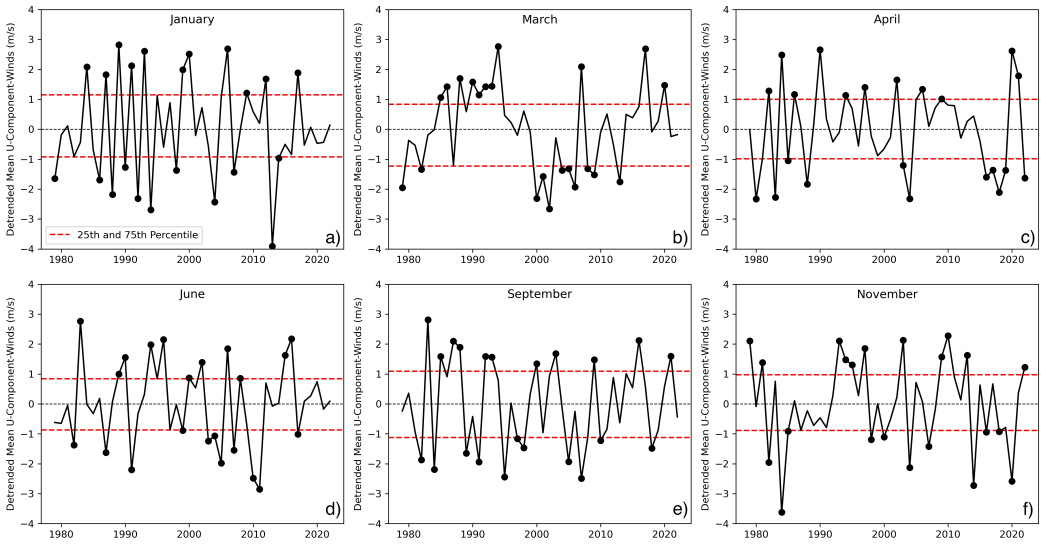

Figure 4. Detrended ERA5 monthly averaged 10m zonal winds (m/s) at Wrangel Island from 1979-2022 for various months. The years used in the composites are indicated by black circle markers. The 75th and 25th percentile cutoffs are denoted with a red dashed line.

same months. Under climatological conditions, there is a reduction in sea ice concentration in the Bering Sea and an increase in the Sea of Okhotsk. In the summer months and in November, there is generally a decrease in ice concentration near the island (Figure 5 d, e, f). We also see a signal near the New Siberian Islands in June and September (Figure 5 d & e), with an increase in ice concentration in the East Siberian Sea and a decrease in the Laptev Sea.

The mean ice thickness difference between months of the strong easterly and westerly winds at Wrangel Island are shown in Figure 6. In the figure, an ice thickness dipole is evident in January, March, April, and June (Figure 6 a, b, c, d). We also see signals near the New Siberian Islands in all months but September. Under climatological easterly flow, the ice is thicker on the eastern side, in the East Siberian Sea, and less thick on the western side, in the Laptev Sea. There are no thickness anomalies in the Bering Sea or the Sea of Okhotsk.

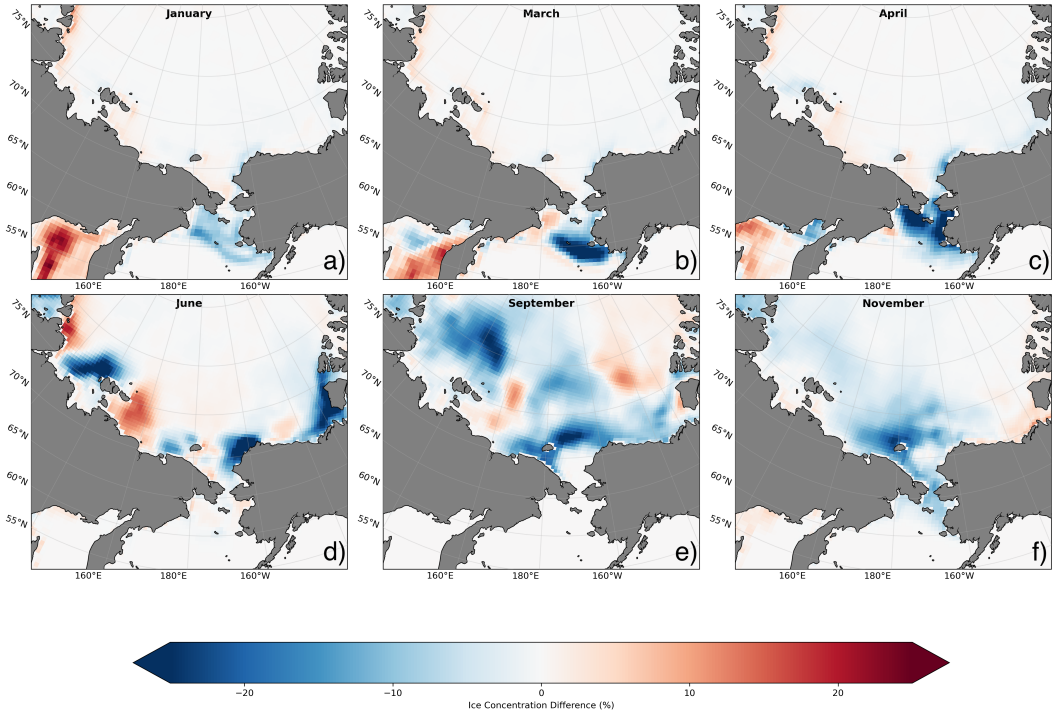

Figure 5. The difference in monthly mean PIOMAS ice concentration (%) between the months of strong easterly and westerly winds at Wrangel Island. This PIOMAS data is from years between 1979-2022.

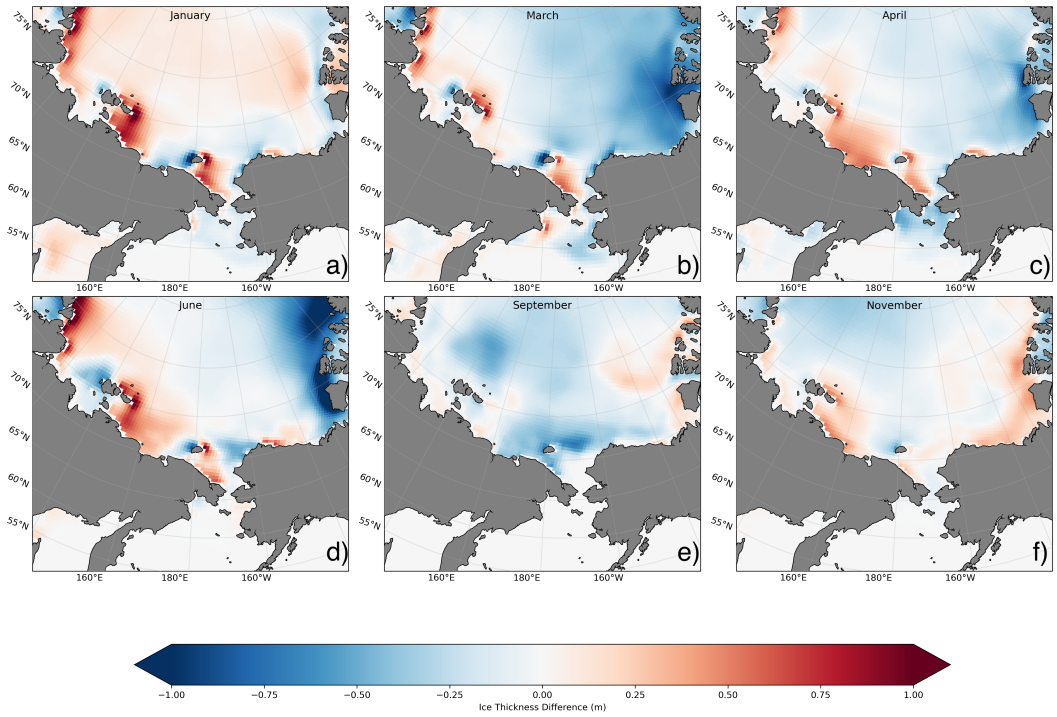

Figure 6. The difference in monthly mean PIOMAS ice thickness (m) fields between months of strong easterly and westerly winds at Wrangel Island for various months. The ice thickness data is from 1979-2022.

Figure 7 shows the same ice thickness difference with a smaller domain, centred on Wrangel Island. In this figure, the dipole appears strongest in January (Figure 7 a), with a maximum ice thickness difference between the eastern and western poles on the order of 2 meters. The lack of sea ice around Wrangel Island in September is evident as Figure 7 e) shows very little ice thickness difference. However, in September we also see a decrease in ice thickness on the east side of the island (Figure 7 e), opposite to the other months which may indicate a reversal in wind direction. Further, in November (Figure 7 f) we see an increase in sea ice thickness on the west side of Alaska, where there is typically a decrease, providing another signal consistent with a reversal in wind direction.

The eastern and western polygons shown in Figure 7 were used to calculate the seasonal cycle of the dipole strength. These polygons are bounded at 70°N and 72.5°N with side boundaries of 175°E and 180°E for the west polygon and 174°W and 179°W for the east polygon. For a particular month, an average of the ice thickness difference over the period 1979-2022 was taken in each polygon and the difference was calculated. This metric of the seasonality of dipole strength is shown in Figure 8. The seasonality of mean ice thickness difference in each polygon is also plotted in Figure 8. Here we confirm the dipole is strongest in January with a mean ice thickness difference of around 1m. Generally, the dipole is strongest in the winter months: December through March, and is weakest in the summer months: July through October. There is a spike in dipole strength in June, perhaps in relation to the seasonal opening of the Wrangel Island Polynya which typically opens in June (Moore & Pickart, 2012). It is evident in the winter that the poles are of approximately equal magnitude, while in June only the western pole is large. This is consistent with the typical opening of the polynya in June.

Next, we investigate potential mechanisms for the presence of this dipole at Wrangel Island. Figure 9 shows the difference in monthly averaged ERA5 sea-level pressure and 10m wind fields triggering off the same months of strong easterly and westerly winds as Figure 7. In all months in Figure 9, there is increased sea-level pressure in the Beaufort

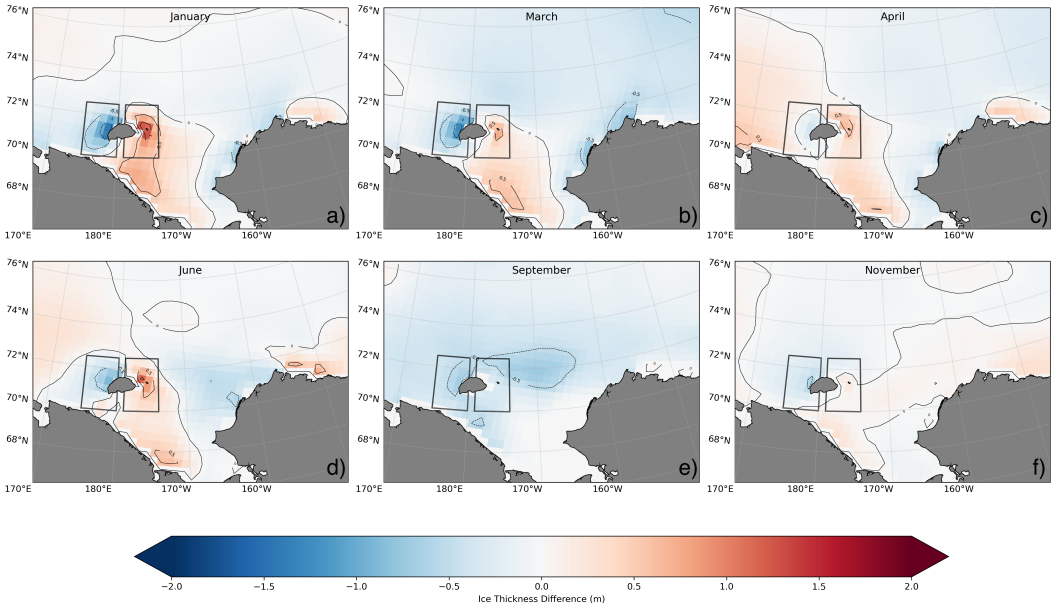

Figure 7. The difference in monthly mean PIOMAS ice thickness (m) fields between months of strong easterly and westerly winds for various months. The ice thickness data is from 1979-2022. The polygons on either side of Wrangel Island are used to calculate the dipole strength. The coordinates bounding the west polygon are 70N to 72.5N and 175E to 180. The coordinates bounding the east polygon are 70N to 72.5N and 174W to 179W.

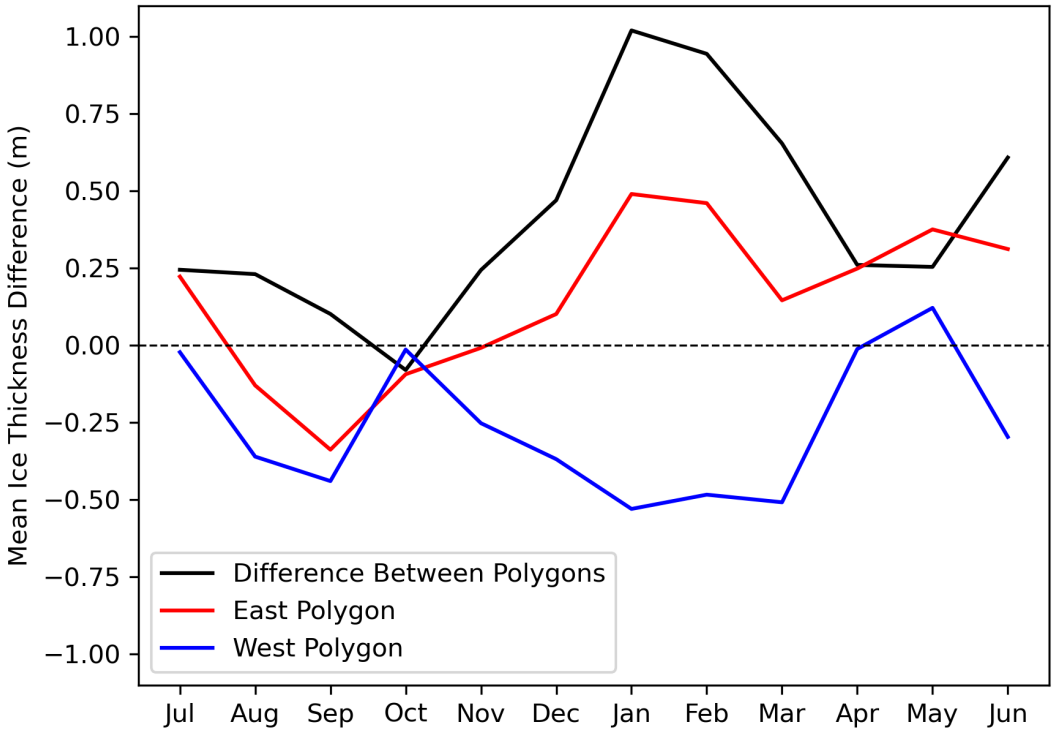

Figure 8. Measure of the strength (m) of the sea ice thickness dipole at Wrangel Island by month. The dipole strength was calculated by taking the difference of the mean ice thickness difference in each polygon from Figure 7 for each month (black line). Also shown is the seasonality of the mean ice thickness difference in the East and West polygons, denoted by the red and blue lines respectively.

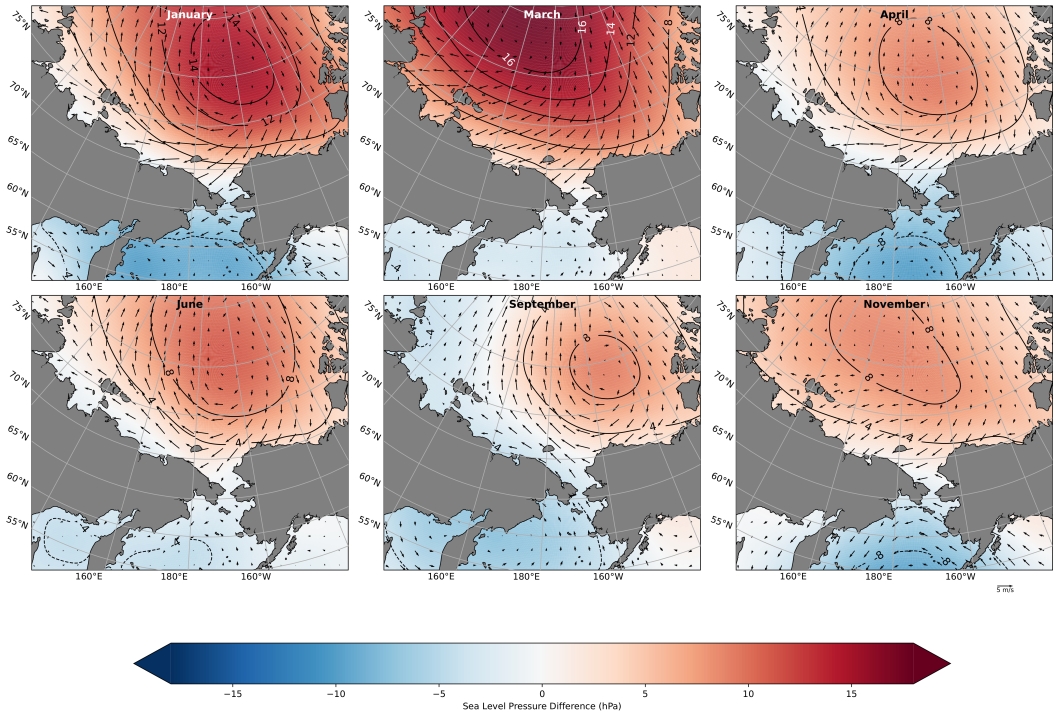

Figure 9. The difference in monthly mean ERA5 sea-level pressure (hPa) fields between months of strong easterly and westerly winds at Wrangel Island for various months. The difference in ERA5 wind vectors (m/s) is also shown. This ERA5 data is from the years between 1979-2022.

Sea extending north toward the Arctic Ocean. Thus, months with the strongest easterly winds at Wrangel Island are associated with an increased BSH. This is consistent with the wind vectors flowing clockwise around the region of increased sea-level pressure. This anticyclonic circulation is consistent with the climatological Beaufort Gyre and forces easterly winds at Wrangel Island. The strongest mean sea-level pressure highs occur in January and March (Figure 9 a & b) with the difference exceeding 14 hPa.

We next examined ice motion from PIOMAS and the NSIDC dataset and its relation to the Wrangel Island dipole. Figure 10 shows the difference in monthly averaged PIOMAS ice motion between months of strong ERA5 easterly and westerly winds. Figure 11 shows the same difference in ice motion using NSIDC data. In both figures, we

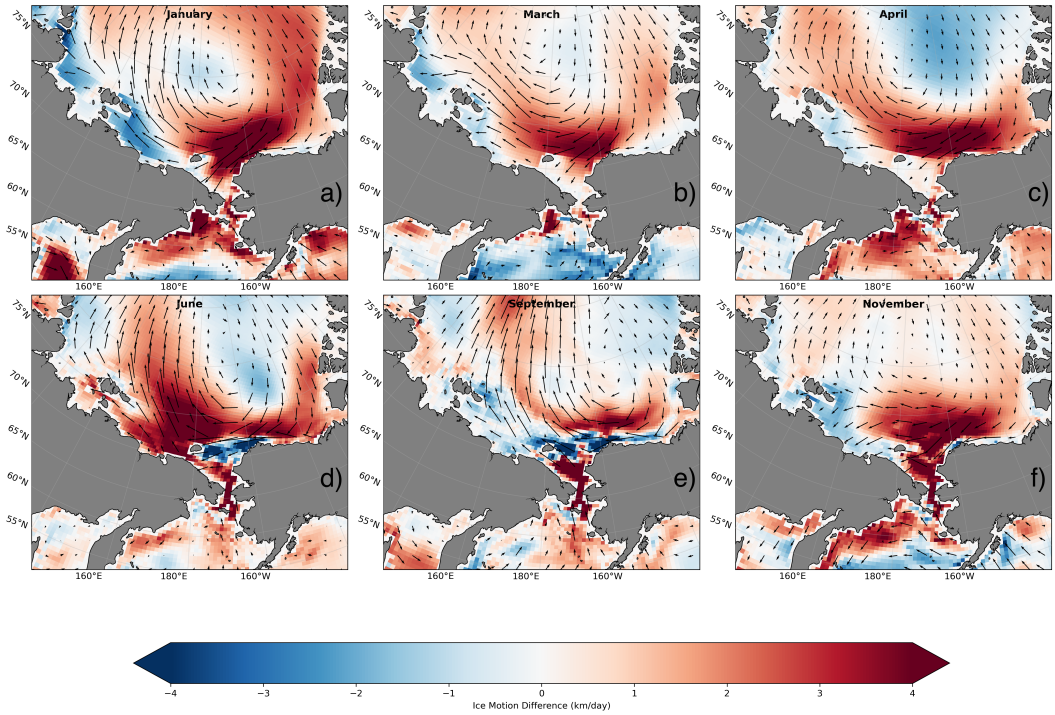

Figure 10. The difference in monthly mean PIOMAS ice motion (km/day) between the months of strong easterly and westerly winds at Wrangel Island. This PIOMAS data is from years between 1979-2022.

find that the ice motion is in general agreement with the ERA5 10m wind motion in Figure 9. Thus, in months of increased easterly winds, there is increased anticyclonic ice motion in the region. In Figures 10 and 11 a), b) and c), it is evident that there is an increase in ice motion towards Wrangel Island from the East and away from the island towards the west. This is consistent with the ice thickness differences due to ice advection in Figure 12. From the NSIDC field in Figure 11, we can see there is little to no ice near Wrangel Island in the summer months through to the early winter (Figure 11 d, e, f). This should be considered when looking at the PIOMAS ice motion field near Wrangel Island during those same months (Figure 10 d, e, f). In regions of no ice concentration, PIOMAS provides the surface current data.

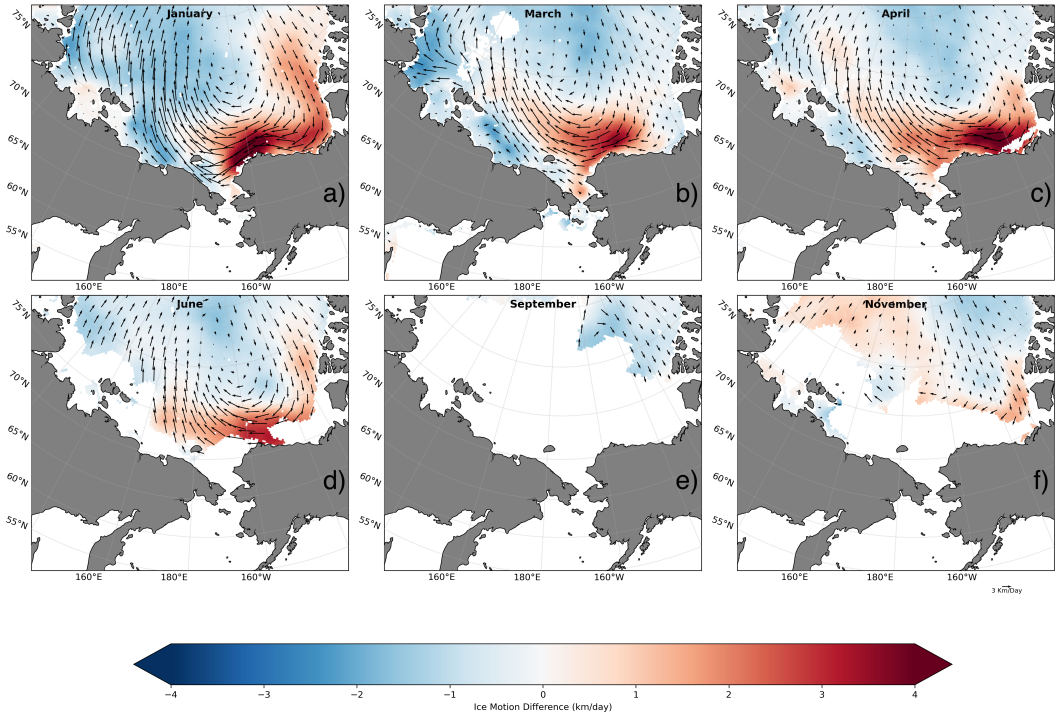

Figure 11. The difference in monthly mean NSIDC ice motion (km/day) between the months of strong easterly and westerly winds at Wrangel Island. This NSIDC data is from years between 1979-2022.

Further, we find sea ice advection plays a large role in the creation of the dipole at Wrangel Island. Figure 12 shows the difference in the monthly mean change in ice thickness due to advection between months of strong easterly and westerly winds. It is evident in all months in Figure 12 that with easterly flow, there is an increase in advection to the east of the island and a decrease to the west of the island. The months with strong easterly winds at Wrangel Island are associated with large ice thickness differences due to ice advection. Thus, strong easterly winds at the island are associated with ice advected towards the island from the east and advected away from the island towards the west. This is consistent with the direction of wind vectors at Wrangel Island in Figure 9 and the direction of ice motion in Figures 10 and 11.

The largest ice thickness difference due to ice advection occurs in January (Figure 12 a) which is consistent with Figures 8 and 9 as January showed the largest increase in sea-level pressure and the strongest ice thickness dipole. In January and April, ice piled up over 1 meter in areas to the east of the island due to ice advection (Figure 12 a & c). Over 1 meter of ice thickness was also advected away from areas on the west side of the island in all months in Figure 12.

We also find ice advection anomalies at the New Siberian Islands between the East Siberian Sea and the Laptev Sea. There are large ice thickness increases due to advection on the east side of the islands in January, March, and April (Figure 12 a, b, c). There are also ice thickness decreases to the west of the islands in the Laptev Sea during those months. These signals are apparent but weaker in June, September, and November (Figure 12 d, e, f). Thus months of strong easterly winds at Wrangel Island are also associated with strong ice advection signals at the New Siberian Islands. This ice advection likely plays a role in the formation of the Great Siberian Polynya and other seasonal polynyas in the Laptev Sea (UN Environment, 2015).

In Figure 13, we show the difference in monthly mean PIOMAS ice thickness due to ice production between the months of strong easterly and westerly winds. There is

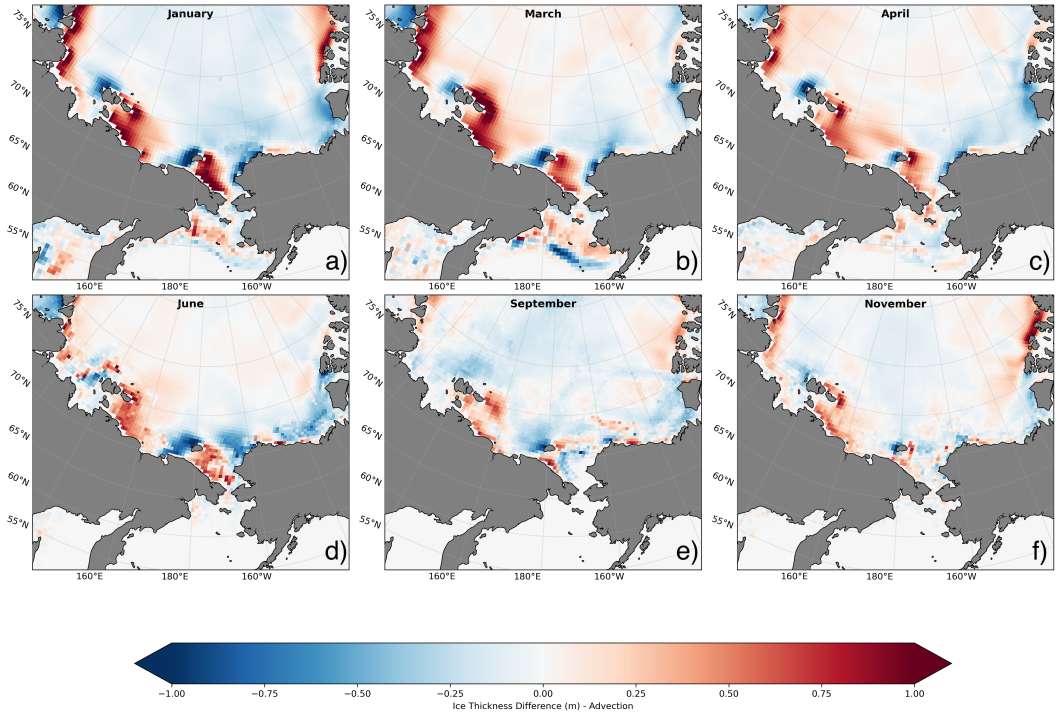

Figure 12. The difference in monthly averaged PIOMAS ice thickness (m) due to ice advection between months of strong easterly and westerly winds at Wrangel Island. This PIOMAS data is from years between 1979-2022.

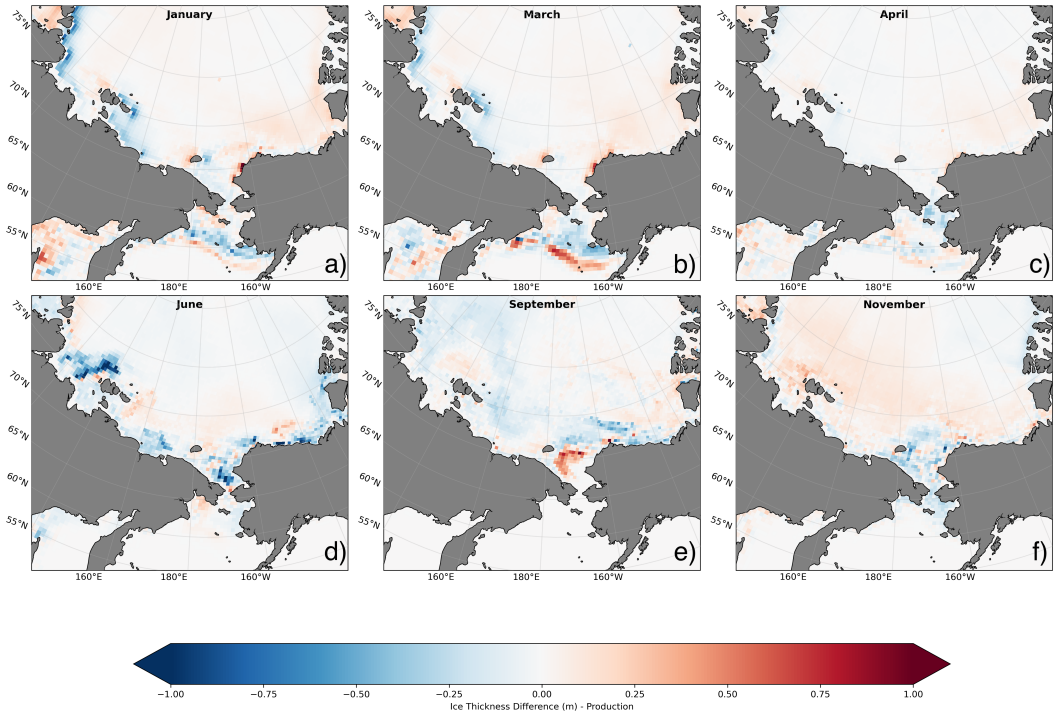

Figure 13. The difference in monthly averaged PIOMAS ice thickness (m) due to ice production between the months of strong easterly and westerly winds at Wrangel Island. This PIOMAS data is from years between 1979-2022.

very little difference in ice thickness due to ice production near Wrangel Island. Thus, the months of the strongest easterly or westerly winds at the island have little relation with ice production. There are, however, some signals near the New Siberian Islands in all months but April (Figure 13 a, b, d, e, f). The strongest signals are found in June (Figure 13 d), where sea ice thickness decreases in the Laptev Sea and the Chukchi Sea due to ice melt. This makes sense as warmer temperatures in June should lead to ice melt.

4 Conclusions

The western Arctic's circulation system is characterized by the Beaufort Gyre which is driven by the climatological anticyclonic surface winds due to the BSH (Ballinger et al., 2021; Timmermans & Toole, 2023). The BSH is critical to many major teleconnec-

tions and to the movement of sea ice and water throughout the western Arctic (Serreze & Barrett, 2011; Serreze & Barry, 2014). Collapses of the BSH and consequent reversals of the Beaufort Gyre have been documented in recent years and have significant impacts on ice motion, ice melt, weather, and biological activity in the region (Ballinger et al., 2021; Babb et al., 2020; Moore et al., 2018).

The climatological BSH and Beaufort Gyre conditions force easterly surface winds and sea ice towards Wrangel Island. Much of this ice is blocked by the island, creating a region of increased ice thickness and pressure ridges to the east of the island. This accumulation of ice was first documented in a 1918 journal article when the shipwrecked crew of the Karluk spent days cutting through ice ridges to get to Wrangel Island (Chafe, 1918). These early in-situ observations have been confirmed with remotely sensed diagnostics of pressure ridge and lead formation ((Hutter et al., 2019; Willmes & Heinemann, 2015). The blockage of ice to the east also contributes to the opening of seasonal polynya to the north-west of Wrangel Island (Sverdrup, 1929; Cavalieri & Martin, 1994; Moore & Pickart, 2012).

We find that reversals in zonal wind direction at Wrangel Island are associated with a sea ice thickness dipole at the island. Under climatological easterly flow, there is an increase in sea ice thickness to the east of the island and a decrease to the west. The sense of the dipole is reversed under westerly flow. This dipole is strongest in January with a mean ice thickness difference of around 1m (Figure 8). The dipole is prominent during the winter months, December through March, and in June (Figure 7 & 8). The spike in dipole strength in June may be related to the formation of the Wrangel Island polynya which typically opens in June (Moore & Pickart, 2012).

Further, we find that strong easterly winds and the sea ice thickness dipole at Wrangel Island are associated with an increased BSH (Figure 9). This BSH increase is strongest in the winter months as shown in Figure 9 a) and b). Accordingly, the dipole is found to be linked to increased anticyclonic ice motion in the region (Figures 10 & 11). This

is consistent with the circulation of the climatological Beaufort Gyre which forces easterly ice motion near Wrangel Island. During these typical conditions, we find the dipole is associated with increased ice advection towards the island from the East and away from the island towards the West (Figure 12). The opposite is true during reversals of the Beaufort Gyre. We also find ice advection signals in the Laptev Sea and East Siberian Sea near the New Siberian Islands. This increased ice advection in the region likely contributes to the formation of seasonal polynyas in the Laptev Sea including the Great Siberian Polynya (UN Environment, 2015). We also find that the ice thickness dipole at Wrangel Island is not associated with changes in ice concentration, production, or melt near the island (Figure 5 & 13).

The lack of a signal of the reversal in wind direction in ice concentration, especially during the winter, is interesting and speaks to the challenges in using this field to characterize ice dynamics. In the presence of 100% ice cover, the response on the eastern side of Wrangel Island to the climatological easterly wind is to thicken the ice without changing the ice concentration. While on the western side, the ice is thinned again without any change in ice concentration as long as the thickness remains non-zero. It is only during the melt season, when there is spatial variability in ice concentration, that a signal of the wind reversal is present in this field.

Future BSH collapses and other Arctic climate changes, such as thinning sea ice, will have impacts on the formation of the sea ice thickness dipole at Wrangel Island. A Beaufort Gyre reversal can cause the dipole to flip as seen in the winter of 2020 (Moore et al., 2022). Changes to the sea ice thickness dipole can impact the formation of the Wrangel Island polynya, and food availability of polar bears and Pacific walrus who live on the island. The basin-wide ocean and sea ice circulation anomalies that drive the dipole may impact the movement of these animals across the western Arctic. In addition, the reversals in the atmospheric circulation that drive the existence of the dipole may impact re-

gional upwelling and downwelling as occurs along the Beaufort Coast (Pickart et al., 2009; Foukal et al., 2019).

5 Open Research

Monthly mean wind and sea-level pressure data from the ERA5 reanalysis are available from the Climate Data Store through the Copernicus Climate Change Service (`https://cds.climate.copernicus.eu/cdsapp#!/home`). The Ostrov Vrangelya (Wrangel Island) station data is available from the National Oceanic and Atmospheric Administration (`https://www.ncei.noaa.gov/access/search/data-search/global-hourly`). Monthly mean ice concentration, ice thickness, ice motion, ice advection, and ice production data are available from the Polar Science Center (`http://psc.apl.uw.edu/research/projects/arctic-sea-ice-volume-anomaly/data/model_grid`). Monthly mean ice motion data is available from the National Snow and Ice Data Center (`https://nsidc.org/data/nsidc-0116/versions/4`).

Acknowledgments

The authors would like to acknowledge support from the Natural Sciences and Engineering Research Council of Canada.

References

Babb, D. G., Landy, J. C., Lukovich, J. V., Haas, C., Hendricks, S., Barber, D. G., & Galley, R. J. (2020, December). The 2017 Reversal of the Beaufort Gyre: Can Dynamic Thickening of a Seasonal Ice Cover During a Reversal Limit Summer Ice Melt in the Beaufort Sea? *Journal of Geophysical Research: Oceans*, *125*(12). Retrieved from https://onlinelibrary.wiley.com/doi/10.1029/2020JC016796 doi: 10.1029/2020JC016796

Ballinger, T. J., Walsh, J. E., Bhatt, U. S., Bieniek, P. A., Tschudi, M. A., Brettschneider, B., ... Shapiro, L. H. (2021, July). Unusual West Arctic Storm Activity During Winter 2020: Another Collapse of the Beaufort High? *Geophysical Research Letters*, *48*(13). Retrieved from https://onlinelibrary.wiley.com/doi/10.1029/2021GL092518 doi: 10.1029/2021GL092518

Bonavita, M., Hólm, E., Isaksen, L., & Fisher, M. (2016, January). The evolution of the ECMWF hybrid data assimilation system. *Quarterly Journal of the Royal Meteorological Society*, *142*(694), 287–303. Retrieved from https://onlinelibrary.wiley.com/doi/10.1002/qj.2652 doi: 10.1002/qj.2652

Cavalieri, D. J., & Martin, S. (1994). The contribution of Alaskan, Siberian, and Canadian coastal polynyas to the cold halocline layer of the Arctic Ocean. *Journal of Geophysical Research*, *99*(C9), 18343. Retrieved from http://doi.wiley.com/10.1029/94JC01169 doi: 10.1029/94JC01169

Chafe, E. F. (1918, May). The Voyage of the "Karluk," and Its Tragic Ending. *The Geographical Journal*, *51*(5), 307. Retrieved from https://www.jstor.org/stable/1780073?origin=crossref doi: 10.2307/1780073

Chinn, S. M., Liston, G. E., & Wilson, R. R. (2023, October). Assessing past and future climatic influences on the availability of polar bear maternal denning habitat on Wrangel Island. *Ecological Modelling*, *484*, 110479. Retrieved from

https://linkinghub.elsevier.com/retrieve/pii/S0304380023002090 doi: 10.1016/j.ecolmodel.2023.110479

Claudino-Sales, V. (2019). Natural System of Wrangel Island Reserve, Russia. In *Coastal World Heritage Sites* (Vol. 28, pp. 209–214). Dordrecht: Springer Netherlands. Retrieved from http://link.springer.com/10.1007/978-94-024-1528-5_31 (Series Title: Coastal Research Library) doi: 10.1007/978-94-024-1528-5_31

Copernicus Climate Change Service. (2019). *ERA5 monthly averaged data on single levels from 1979 to present* [dataset]. ECMWF. Retrieved from https://cds.climate.copernicus.eu/doi/10.24381/cds.f17050d7 doi: 10.24381/CDS.F17050D7

Foukal, N. P., Pickart, R. S., Moore, G. W. K., & Lin, P. (2019, October). Shelfbreak Downwelling in the Alaskan Beaufort Sea. *Journal of Geophysical Research: Oceans*, *124*(10), 7201–7225. Retrieved from https://onlinelibrary.wiley.com/doi/10.1029/2019JC015520 doi: 10.1029/2019JC015520

Frey, K. E., Moore, G., Cooper, L. W., & Grebmeier, J. M. (2015, August). Divergent patterns of recent sea ice cover across the Bering, Chukchi, and Beaufort seas of the Pacific Arctic Region. *Progress in Oceanography*, *136*, 32–49. Retrieved from https://linkinghub.elsevier.com/retrieve/pii/S0079661115001068 doi: 10.1016/j.pocean.2015.05.009

Hamilton, C. D., Lydersen, C., Aars, J., Acquarone, M., Atwood, T., Baylis, A., ... Kovacs, K. M. (2022, December). Marine mammal hotspots across the circumpolar Arctic. *Diversity and Distributions*, *28*(12), 2729–2753. Retrieved from https://onlinelibrary.wiley.com/doi/10.1111/ddi.13543 doi: 10.1111/ddi.13543

Hersbach, H., Bell, B., Berrisford, P., Hirahara, S., Horányi, A., Muñoz-Sabater, J., ... Thépaut, J. (2020, July). The ERA5 global reanalysis. *Quarterly Journal of the Royal Meteorological Society*, *146*(730), 1999–2049. Retrieved

from https://onlinelibrary.wiley.com/doi/10.1002/qj.3803 doi: 10.1002/qj.3803

Hutter, N., Zampieri, L., & Losch, M. (2019, February). Leads and ridges in Arctic sea ice from RGPS data and a new tracking algorithm. *The Cryosphere*, *13*(2), 627–645. Retrieved from https://tc.copernicus.org/articles/13/627/2019/ doi: 10.5194/tc-13-627-2019

Jay, C., Fischbach, A., & Kochnev, A. (2012, November). Walrus areas of use in the Chukchi Sea during sparse sea ice cover. *Marine Ecology Progress Series*, *468*, 1–13. Retrieved from http://www.int-res.com/abstracts/meps/v468/p1-13/ doi: 10.3354/meps10057

Kalnay, E., Kanamitsu, M., Kistler, R., Collins, W., Deaven, D., Gandin, L., ... Joseph, D. (1996, March). The NCEP/NCAR 40-Year Reanalysis Project. *Bulletin of the American Meteorological Society*, *77*(3), 437–471. Retrieved from http://journals.ametsoc.org/doi/10.1175/1520-0477(1996)077<0437:TNYRP>2.0.CO;2 doi: 10.1175/1520-0477(1996)077⟨0437:TNYRP⟩2.0.CO;2

Kendall, M. (1948). *Rank correlation methods*. Oxford, England: Griffin.

LaRue, M. A., & Stapleton, S. (2018, December). Estimating the abundance of polar bears on Wrangel Island during late summer using high-resolution satellite imagery: a pilot study. *Polar Biology*, *41*(12), 2621–2626. Retrieved from http://link.springer.com/10.1007/s00300-018-2384-4 doi: 10.1007/s00300-018-2384-4

Mann, H. B. (1945, July). Nonparametric Tests Against Trend. *Econometrica*, *13*(3), 245. Retrieved from https://www.jstor.org/stable/1907187?origin=crossref doi: 10.2307/1907187

Moore, G., & Pickart, R. S. (2012, March). The Wrangel Island Polynya in early summer: Trends and relationships to other polynyas and the Beaufort Sea High: THE EARLY SUMMER WRANGEL ISLAND POLYNYA. *Geophysical Research Letters*, *39*(5), n/a–n/a. Retrieved from http://doi.wiley.com/

10.1029/2011GL050691 doi: 10.1029/2011GL050691

Moore, G., Schweiger, A., Zhang, J., & Steele, M. (2018, March). Collapse of the 2017 Winter Beaufort High: A Response to Thinning Sea Ice? *Geophysical Research Letters*, *45*(6), 2860–2869. Retrieved from https://onlinelibrary.wiley.com/doi/10.1002/2017GL076446 doi: 10.1002/2017GL076446

Moore, G., Steele, M., Schweiger, A. J., Zhang, J., & Laidre, K. L. (2022, August). Thick and old sea ice in the Beaufort Sea during summer 2020/21 was associated with enhanced transport. *Communications Earth & Environment*, *3*(1), 198. Retrieved from https://www.nature.com/articles/s43247-022-00530-6 doi: 10.1038/s43247-022-00530-6

NOAA National Centers for Environmental Information. (2001). *Global surface hourly wind - observation* [dataset]. NOAA National Centers for Environmental Information. Retrieved from https://www.ncei.noaa.gov/access/search/data-search/global-hourly

Pfirman, S. (2004). Variability in Arctic sea ice drift. *Geophysical Research Letters*, *31*(16), L16402. Retrieved from http://doi.wiley.com/10.1029/2004GL020063 doi: 10.1029/2004GL020063

Pickart, R. S., Moore, G. W. K., Torres, D. J., Fratantoni, P. S., Goldsmith, R. A., & Yang, J. (2009, September). Upwelling on the continental slope of the Alaskan Beaufort Sea: Storms, ice, and oceanographic response. *Journal of Geophysical Research*, *114*, C00A13. Retrieved from http://doi.wiley.com/10.1029/2008JC005009 doi: 10.1029/2008JC005009

Rigor, I. G., Wallace, J. M., & Colony, R. L. (2002, September). Response of Sea Ice to the Arctic Oscillation. *Journal of Climate*, *15*(18), 2648–2663. Retrieved from http://journals.ametsoc.org/doi/10.1175/1520-0442(2002)015<2648:ROSITT>2.0.CO;2 doi: 10.1175/1520-0442(2002)015⟨2648:ROSITT⟩2.0.CO;2

Schweiger, A. J., Lindsay, R., Zhang, J., Steele, M., Stern, H., & Kwok, R. (2011, September). Uncertainty in modeled Arctic sea ice volume. *Journal of Geophysical Research*, *116*, C00D06. Retrieved from http://doi.wiley.com/10.1029/2011JC007084 doi: 10.1029/2011JC007084

Schweiger, A. J., & Zhang, J. (2015, December). Accuracy of short-term sea ice drift forecasts using a coupled ice-ocean model. *Journal of Geophysical Research: Oceans*, *120*(12), 7827–7841. Retrieved from https://onlinelibrary.wiley.com/doi/abs/10.1002/2015JC011273 doi: 10.1002/2015JC011273

Serreze, M. C., & Barrett, A. P. (2011, January). Characteristics of the Beaufort Sea High. *Journal of Climate*, *24*(1), 159–182. Retrieved from http://journals.ametsoc.org/doi/10.1175/2010JCLI3636.1 doi: 10.1175/2010JCLI3636.1

Serreze, M. C., & Barry, R. G. (2014). *The Arctic climate system* (Second edition ed.). New York, NY, USA: Cambridge University Press.

Smith, A., Lott, N., & Vose, R. (2011). The Integrated Surface Database. *American Meteorological Society*, *92*(6), 704–708. doi: DOI:10.1175/2011BAMS3015.1

Student. (1908, March). The Probable Error of a Mean. *Biometrika*, *6*(1), 1. Retrieved from https://www.jstor.org/stable/2331554?origin=crossref doi: 10.2307/2331554

Sverdrup, H. U. (1929). *The waters on the North-Siberian Shelf* (Vol. 4) (No. 2). Geofysisk Institutt, Bergen.

Timmermans, M.-L. E., & Pickart, R. S. (2023, July). The Arctic Ocean's Changing Beaufort Gyre System: An Assessment of Current Understanding, Open Questions and Future Research Directions. *Bulletin of the American Meteorological Society*, *104*(7), E1282–E1289. Retrieved from https://journals.ametsoc.org/view/journals/bams/104/7/BAMS-D-23-0129.1.xml doi: 10.1175/BAMS-D-23-0129.1

Timmermans, M.-L. E., & Toole, J. M. (2023, January). The Arctic Ocean's Beaufort Gyre. *Annual Review of Marine Science*, *15*(1), 223–248. Retrieved from

https://www.annualreviews.org/doi/10.1146/annurev-marine-032122-012034 doi: 10.1146/annurev-marine-032122-012034

Tschudi, M. A., Meier, W. N., & Stewart, J. S. (2020, May). An enhancement to sea ice motion and age products at the National Snow and Ice Data Center (NSIDC). *The Cryosphere*, *14*(5), 1519–1536. Retrieved from https://tc.copernicus.org/articles/14/1519/2020/ doi: 10.5194/tc-14-1519-2020

Tschudi, M. A., & Univ Of CO. (2019). *Polar Pathfinder Daily 25 km EASE-Grid Sea Ice Motion Vectors* [dataset]. NASA National Snow and Ice Data Center Distributed Active Archive Center. Retrieved from http://nsidc.org/data/nsidc-0116/versions/4 doi: 10.5067/INAWUWO7QH7B

UN Environment. (2015, June). *Ecologically or Biologically Significant Areas (EBSAs) Great Siberian Polynya.* UN Environment. Retrieved from https://chm.cbd.int/database/record?documentID=204097

Willmes, S., & Heinemann, G. (2015, December). Sea-Ice Wintertime Lead Frequencies and Regional Characteristics in the Arctic, 2003–2015. *Remote Sensing*, *8*(1), 4. Retrieved from http://www.mdpi.com/2072-4292/8/1/4 doi: 10.3390/rs8010004

Zhang, J., Lindsay, R., Schweiger, A. J., & Rigor, I. (2012, October). Recent changes in the dynamic properties of declining Arctic sea ice: A model study. *Geophysical Research Letters*, *39*(20), 2012GL053545. Retrieved from https://onlinelibrary.wiley.com/doi/abs/10.1029/2012GL053545 doi: 10.1029/2012GL053545

Zhang, J., & Rothrock, D. A. (2003, May). Modeling Global Sea Ice with a Thickness and Enthalpy Distribution Model in Generalized Curvilinear Coordinates. *Monthly Weather Review*, *131*(5), 845–861. Retrieved from http://journals.ametsoc.org/doi/10.1175/1520-0493(2003)131<0845:MGSIWA>2.0.CO;2 doi: 10.1175/1520-0493(2003)131⟨0845:MGSIWA⟩2.0.CO;2